WATER

Experimental evidence of a liquid-liquid critical point in supercooled water

Seonju You[1]†, Marjorie Ladd-Parada[2,3]†, Kyeongmin Nam[1], Aigerim Karina[2], Seoyoung Lee[1], Myeongsik Shin[1], Cheolhee Yang[1], Yeseul Han[1], Sangmin Jeong[1], Kichan Park[1], Kyeongwon Kim[1], Minjeong Ki[1], Robin Tyburski[2], Iason Andronis[2], Keely Ralf[4], Jae Hyuk Lee[5], Intae Eom[5], Minseok Kim[5], Rory Ma[5], Dogeun Jang[5], Fivos Perakis[2], Peter H. Poole[4], Katrin Amann-Winkel[2,6,7], Kyung Hwan Kim[1]*, Anders Nilsson[2]*

The search for the liquid-liquid critical point in supercooled water is challenging owing to rapid crystallization. We studied supercooled water at timescales before ice formation by heating high- and low-density amorphous ices using infrared ultrafast laser pulses, followed by x-ray scattering. By varying the pump laser fluence, we accessed liquid states straddling the predicted critical point. We observed a crossover from a discontinuous to a continuous transition at which broad and slow structural variations occurred, consistent with critical fluctuations and slowing down. We also observed a rapid increase in the heat capacity indicating a critical divergence at 210 ± 8 K coincident with enhanced density fluctuations. These results suggest that our experiments have directly probed the vicinity of a critical point in supercooled water.

Water is notable for its many anomalies, such as a density maximum at 277 K. These anomalies grow upon cooling below the freezing point into the metastable supercooled regime (*1*). In particular, the apparent divergence of water's isothermal compressibility (κ_T) (*2*), heat capacity (C_P) (*3*), and correlation length (ζ) (*4*) approaching a temperature of 228 K has resulted in an intense search for the origin of this anomalous behavior.

In 1992, a bold hypothesis proposed that water's anomalies are caused by a second critical point, influencing a large region of the water phase diagram (*5*). In this proposal, a liquid-liquid transition (LLT) in supercooled water, occurring between high-density liquid (HDL) and low-density liquid (LDL) phases (*5*–*8*), terminates at a liquid-liquid critical point (LLCP). The proposed LLCP occurs at positive pressure, and so at lower and ambient pressure, no discontinuous transition is observed (*5*, *9*). Other scenarios have been proposed for water's divergent thermodynamic response functions (*10*–*13*), but experiments have shown inconsistencies with these hypotheses (*8*, *14*–*24*). Several molecular dynamics (MD) simulations exhibit a LLCP, but with a large variation, depending on the water model, in its location in terms of pressure and temperature (P_c and T_c) (*9*, *25*–*28*). Theoretical two-state modeling and extrapolation of water's thermodynamic properties also support the existence of a LLCP (*29*–*31*).

Direct experimental observation of the LLCP is extremely challenging because, at its predicted location in the water phase diagram, ice crystallization occurs on a microsecond timescale (*8*, *18*, *20*). However, recent experiments, exploiting ultrafast techniques to rapidly change temperature and pressure and then probe the liquid structure, have successfully studied bulk liquid water under these conditions (*8*, *15*–*18*, *20*, *21*, *24*). These experiments have observed a HDL-to-LDL phase transition at positive pressure (*8*, *15*), continuous phase behavior at 1 bar at temperatures down to 228 K (*16*, *17*, *21*, *24*), and the presence of maxima in several thermodynamic response functions at 1 bar and 230 K (*16*, *17*).

In previous experiments that investigated the LLT by pumping amorphous ices with infrared (IR) femtosecond laser light, the intense ultrashort pulse induced additional excitations of the electron system due to multiphoton nonlinear effects, and not all deposited energy contributed to vibrational heating (*8*, *15*). In this study, we instead used a nanosecond IR laser where the pulse length is 10^5 times larger (using a 5-ns pulse duration), thereby eliminating any nonlinear effects and allowing all deposited energy to be channeled into vibrational heating. The resulting increased heating power enabled both high-density amorphous ice (HDA) and low-density amorphous ice (LDA) to be laser-pumped to higher temperatures that include the predicted region of the LLCP.

Experimental design

The experiments were performed by mounting HDA and LDA samples in a cryostat inside a vacuum chamber and carrying out pump-probe measurements in transmission geometry using IR and x-ray laser beams (fig. S1) (*32*). The procedure was similar to previous studies (*8*, *15*), except for the usage of a nanosecond IR laser for heating the sample and, in a few experiments, a combination of both nano- and femtosecond IR laser beams, at 2-μm wavelength. By keeping both the HDA (115 K) and LDA (135 K) samples at or slightly above their glass transition temperatures before pumping, the sample was already in its ultraviscous liquid state. The samples were heated to a liquid, approximately along an isochore on a timescale of nanoseconds, followed by a decompression process on a longer timescale. Simulations have confirmed fast liquid-like diffusion at temperatures around 200 K on timescales of <20 ps after rapid heating of the amorphous state (*8*). After heating, each sample was probed with a 50-fs x-ray pulse at 9.5 keV at a chosen time delay after the IR pump pulse, ranging from 12.6 ns up to the microsecond timescale, and the x-ray scattering pattern was recorded. The sample was moved to a fresh position for each pump-probe shot.

Figure 1A shows a schematic pressure-temperature (*P*-*T*) phase diagram for supercooled water, displaying the HDL-LDL binodal, the HDL and LDL spinodals, the LLCP, and a supercritical region. The arrows illustrate the approximate experimental process for HDA, initiated with approximate isochoric heating, followed by isothermal decompression to lower pressure at various temperatures below and above T_c, depending on the fluence of the IR laser pump. Figure 1B shows schematic plots of Gibbs free energy versus density corresponding to the phase behavior in Fig. 1A, at different times as pressure decreases during decompression, consistent with results of recent MD simulations (*27*, *28*, *33*). These plots depict the time evolution of the sample density, initially in the HDL phase immediately after heating, in terms of how the free energy surface changes along the decompression paths in Fig. 1A. At a low temperature (T_1), there is a barrier between the LDL and HDL basins throughout decompression, and so the phase transition occurs through nucleation and growth, generating slowly growing LDL domains. When the temperature is higher (T_2), slightly below T_c, the HDL basin disappears during decompression, and spinodal decomposition occurs, with rapid development of small LDL domains (*34*). At T_c (T_3), and at pressures close to the LLCP, there is a negligible free energy barrier, creating critical HDL and LDL domains with a wide range of length scales. Above T_c (T_4), there is only a single liquid basin, with supercritical fluctuations, and the density of the free

[1]Department of Chemistry, POSTECH, Pohang, Republic of Korea. [2]Department of Physics, AlbaNova University Center, Stockholm University, Stockholm, Sweden. [3]Department of Chemistry, KTH Royal Institute of Technology, Stockholm, Sweden. [4]Department of Physics, St. Francis Xavier University, Antigonish, Nova Scotia, Canada. [5]Pohang Accelerator Laboratory, Pohang, Gyeongbuk, Republic of Korea. [6]Max Planck Institute for Polymer Research, Mainz, Germany. [7]Institute of Physics, Johannes Gutenberg University Mainz, Mainz, Germany. ***Corresponding author. Email: kimkyunghwan@postech.ac.kr (K.H.K.); andersn@fysik.su.se (A.N.)**
†These authors contributed equally to this work.

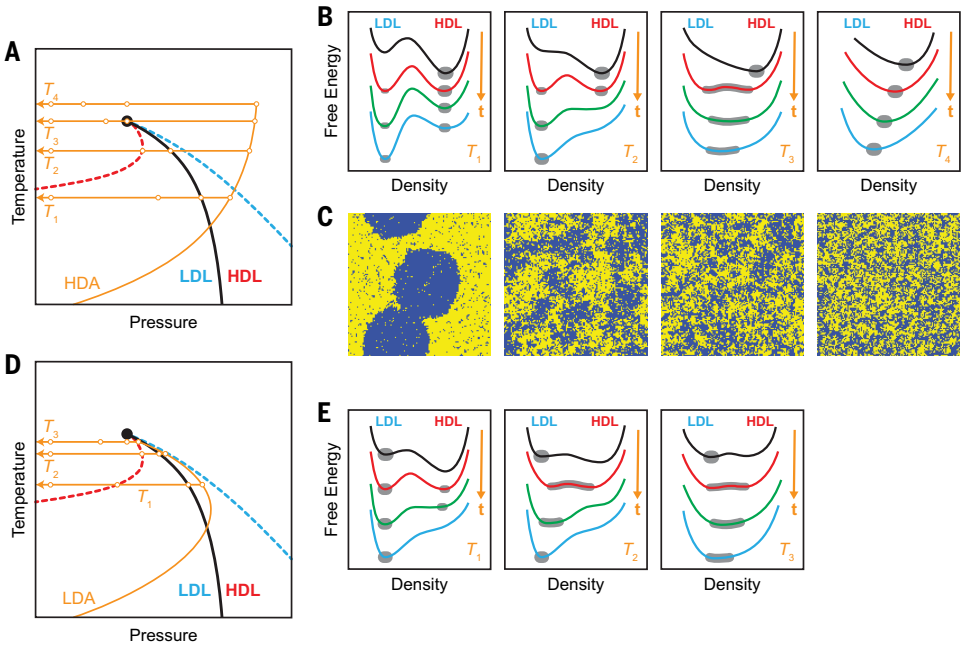

Fig. 1. The experimental approach to the LLT and LLCP. (**A**) A hypothetical water *P-T* phase diagram showing the HDL-LDL binodal line (black solid line), the HDL and LDL spinodals (dashed lines, red and blue, respectively), and the LLCP (black circle). The orange line and arrows show approximate isochoric heating of HDA to four different temperatures, followed by decompression to 1 bar. (**B**) Schematic representation of the Gibbs free energy versus density during decompression at the four temperatures shown in (A). In each panel, the evolution with time *t* of the free energy is shown, from top to bottom, after the heating (black), near the coexistence of HDL and LDL (red), evolving toward the final pressure (green), and at the final pressure after decompression is complete (blue). For each curve, the range of densities manifested in the sample are indicated in gray. The height of the free energy barrier in the vicinity of the critical point is on the order of k_T or less, where *k* is Boltzmann's constant. (**C**) Cross sections of 3D Ising model configurations at the midpoint of the transition from the initial phase (yellow) to the final phase (blue) following isothermal paths analogous to those shown in (A), at different temperatures above and below the critical temperature (T_c). These images provide a course-grained snapshot of the various processes that occur along the decompression paths in (A), showing (from left to right) nucleation at $T = 0.7\ T_c$, spinodal decomposition or nucleation at $0.95\ T_c$, critical fluctuations at T_c, and supercritical fluctuations at $T = 1.1\ T_c$. Note that the difference between T_c and $1.1\ T_c$ is subtle, but the former shows regions with larger domain sizes owing to critical fluctuations on all length scales. (**D**) Same as in (A), but showing heating of LDA to three different temperatures close to the LLCP, followed by decompression to 1 bar. (**E**) Schematic representation of the evolution of the Gibbs free energy during decompression at the three temperatures shown in (D). The color of each curve has the same meaning as in (B).

energy minimum decreases during decompression. The characteristic coarse-grained structure of the system in these four cases is illustrated in Fig. 1C using the three-dimensional (3D) Ising model. The Ising model exhibits an archetypal first-order phase transition, terminating at a critical point belonging to the same universality class predicted for the LLCP in water. Figure 1C shows example slices through the Ising system at the halfway point of the phase transition under conditions analogous to each of the four paths shown in Fig. 1A (*32*). We tested for the signatures of the behavior predicted in Fig. 1, A to C, in our HDA heating experiments, as revealed by the first peak in the structure factor of wide-angle x-ray scattering (WAXS) and in the low momentum transfer (*q*) region of small-angle x-ray scattering (SAXS).

Figure 1D shows the *P-T* phase diagram depicting the experimental process for LDA. Figure 1E shows the evolution of the free energy corresponding to several decompression paths that follow heating of LDA. Isochoric heating of LDA resulted in the formation of HDL domains, which was ascribed to crossing the binodal (*15*), as depicted at T_1 in Fig. 1D. The density of LDA (0.94 g/cm^3) is closer than that of HDA (1.17 g/cm^3) to the predicted critical density (ρ_c) of the LLCP (1.023 ± 0.007 g/cm^3; see Discussion). Therefore, the additional heating with the nanosecond laser may bring the LDA sample close to the *P-T* conditions of the LLCP, resulting in sampling of a wide range of densities after heating and during decompression, as illustrated at T_2 and T_3 in Fig. 1, D and E. These predictions were tested using the high fluence conditions in our experiments.

X-ray scattering of HDA

Figure 2 shows the x-ray scattering signals of HDA at different pump-probe delays in the *q* ranges of WAXS and SAXS for four different pump laser fluences (*32*). Figure 2A shows the WAXS signal at a fluence of 3 J/cm^2. The peak position before heating was at $q = 2.1$ Å^{-1} (fig. S2) (*32*), in good agreement with recent x-ray studies (*8*, *35*–*37*). At later delays, the peak position remained constant but decreased in intensity, and, simultaneously, a shoulder appeared at $q = 1.7$ Å^{-1}, corresponding to the *q* position of LDA (*8*, *35*–*37*). The position and intensity of the 1.7 Å^{-1} feature are consistent with (*8*) at the maximum fluence of the femtosecond IR laser used in that study, suggesting that the nanosecond laser used in this study deposits equivalent energy (fig. S3) (*32*). The SAXS signal at the 3 J/cm^2 fluence (Fig. 2B) shows a weak maximum enhancement at 25 ns. If there are growing LDL domains at longer delays, as indicated by the WAXS signal, then they are likely so large that their SAXS signature appears at lower *q* values outside our detection window.

Figure 2C shows the WAXS signal when the fluence was increased to 11 J/cm^2, and it is similar to Fig. 2A, but with much faster and complete transformation to LDL at 1 μs. Comparison with the transformation rate found with femtosecond heating (*38*) suggests that the transition in Fig. 2C occurs ~100 times faster, indicating that 11 J/cm^2 accesses lower-viscosity liquid states and a lower, and perhaps vanishing, LLT free energy barrier, consistent with a crossover from nucleation to spinodal decomposition. We also note that the LDL WAXS peak at 1 μs exhibits clear asymmetry at higher *q* values, which is not seen in LDA but is typically observed in liquid states at temperatures of >200 K (*18*, *24*, *32*, *39*, *40*) (fig. S24). Figure 2D shows the SAXS curves at 11 J/cm^2, which exhibit much stronger and persistent enhancement within our *q* range than in Fig. 2B.

As the laser fluence increased to 15 J/cm^2 (the maximum power of the nanosecond IR laser), the WAXS signature of two distinct liquids was less evident, as shown in Fig. 2E. At the first delay (12.6 ns), the HDL-related peak decreased in height and broadened as the intensity grew around 1.7 Å^{-1}. At longer delays (50 to 200 ns), a single broad feature centered at a *q* position between HDL and LDL was observed, with only small changes occurring at later times. Additionally, Fig. 2F shows that the increase in SAXS intensity was much stronger compared with lower fluences. The maximum SAXS intensity occurred at 200 ns, and not at the longest delay, indicating that the maximum peak intensity had passed during decompression.

Further change in system behavior occurred as the laser fluence increased to 20 J/cm^2 (the maximum combined power of the nano- and femtosecond lasers), as shown in Fig. 2G. The WAXS signal showed a continuous shift from HDL at early delays, to *q* positions between HDL

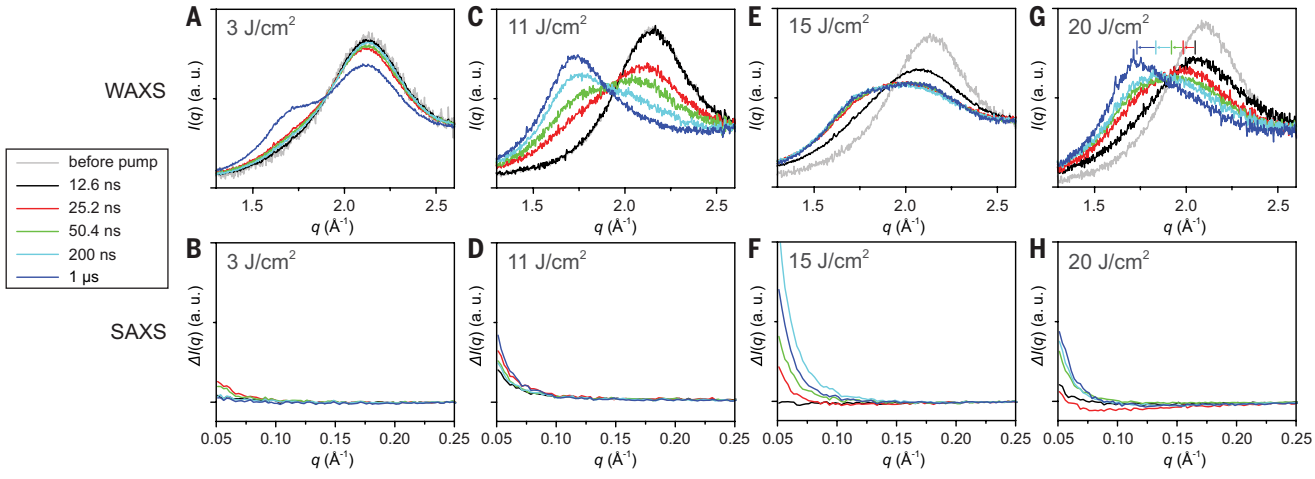

Fig. 2. X-ray scattering during the decompression process of HDA at different laser fluences. (**A**, **C**, **E**, and **G**) Experimental WAXS intensities around the first peak in the structure factor at different delays after laser pumping of HDA at 3, 11, 15, and 20 J/cm^2 laser fluence. (**B**, **D**, **F**, and **H**) Experimental SAXS intensities between $q = 0.05$ to 0.25 Å^{-1} at the same delays and laser fluences as in (A), (C), (E), and (G). The intensity scales are the same for (A), (C), (E), and (G) and for (B), (D), (F), and (H), respectively. a. u., arbitrary units.

and LDL at intermediate delays ($q = 1.9$ Å^{-1} at 200-ns delay), and toward the LDL scattering curve, but with a greater asymmetry at 1 μs. The SAXS signal showed a smaller maximum enhancement in comparison to that at 15 J/cm^2 laser fluence.

To estimate the temperature reached using different fluences, we analyzed the q position of the LDL phase at the end of decompression and compared it with the corresponding position from a recent ultrafast electron diffraction study of rapidly cooled water at 1 bar (fig. S7) (*32*). We estimated that the temperature at 3 J/cm^2 is 205 K, at 11 J/cm^2 is 210 K, at 15 J/cm^2 is 213 K, and at 20 J/cm^2 is 213 K. The error in each temperature estimate is less than ±4 K. However, these temperature estimates obtained after decompression represent an upper limit, as heating can occur during sample expansion (*26*).

Temperature and heat capacity estimation after heating LDA

In the case of heating LDA, the Bragg shift of the ice formed after crystallization can be used to determine the temperature reached after heating at different fluences (*8*). Approximately 10 pump-probe shots were used to estimate the temperature at each fluence (fig. S8) (*32*). Figure 3A shows the average Bragg shift as a function of laser fluence. We determined the relationship between the absolute temperature and the Bragg shift using a comparison of electron diffraction data measured on cold water (*24*) and x-ray scattering of the fully compressed HDA (fig. S8) (*32*). The absolute temperature of the heated LDA was estimated using this relationship. Figure 3A shows a rapid increase in temperature up to 5 J/cm^2, after which the temperature plateaus at higher fluences. Despite the large increase in deposited energy, the sample temperature increased slowly, implying a rapid increase in the heat capacity at higher fluences.

Although laser heating occurs approximately isochorically, after heating, the system is free to explore density fluctuations and the average density changes during decompression, and so we assume that the sample temperature established by the heating energy Q is controlled by the isobaric heat capacity $C_P = dQ/dT$. Along the critical isobar approaching the LLCP, C_P is expected to obey a power law with a critical exponent $\gamma = 1.26$, as predicted for the 3D Ising universality class (*41*)

$$C_P = \frac{dQ}{dT} = a\left(T_c - T\right)^{-\gamma} + c \quad (1)$$

where a and c are constants.

To test whether the observed relation between heating energy and temperature is consistent with the approach to a LLCP, we derived a fitting function for the fluence as a function of temperature and fit this using the temperature values obtained from analyzing Fig. 3A (*32*). The result is shown in Fig. 3B, demonstrating that the data are in line with a power law divergence of C_P, with a best-fit value for T_c of 210 ± 8 K. We note that the data in Fig. 3B are obtained by heating samples to various temperatures along a near-critical isochore rather than the critical isobar. Nonetheless, the qualitative behavior, in which C_P increases strongly as the temperature increases, is consistent with the approach to a LLCP at the highest fluence studied here.

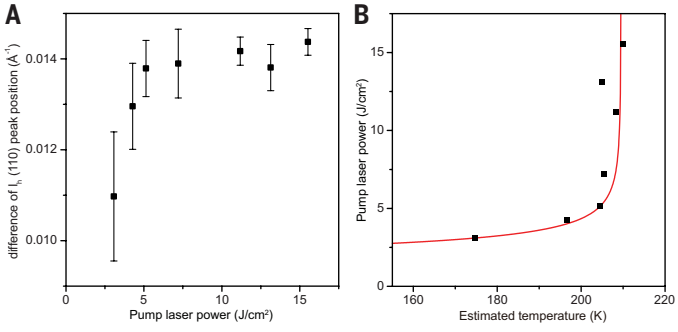

Fig. 3. Determination of temperature reached after laser heating of LDA. (**A**) The shift of the ice Bragg peaks after crystallization as a function of laser fluence, at a delay of 30 μs. The error bars indicate the standard deviation of the data from ~10 independent measurements, and the filled squares indicate the average. (**B**) Laser energy versus the average of estimated temperatures based on the shift of the ice Bragg peaks after crystallization. The absolute temperature was determined by comparing the shift in ice to the Bragg shifts of HDA, where a previous electron diffraction study enabled a comparison to the temperature of the liquid before crystallization (see main text). A power law (red curve) based on Eq. 1 is fitted to the average temperature data to test for a divergence in C_P. The estimated divergence temperature from the fit is 210 ± 8 K.

X-ray scattering of LDA

Figure 4, A to C, shows the WAXS signal for LDA obtained at various delays, for three different laser fluences (*32*). Figure 4A shows the WAXS data at a fluence of 4 J/cm^2. The peak position before heating is at $q = 1.7$ Å^{-1} (*32*), in good agreement with recent studies on LDA. At short delays, a weak shoulder appears at the position of HDA, as was observed in the previous study using a femtosecond IR laser,

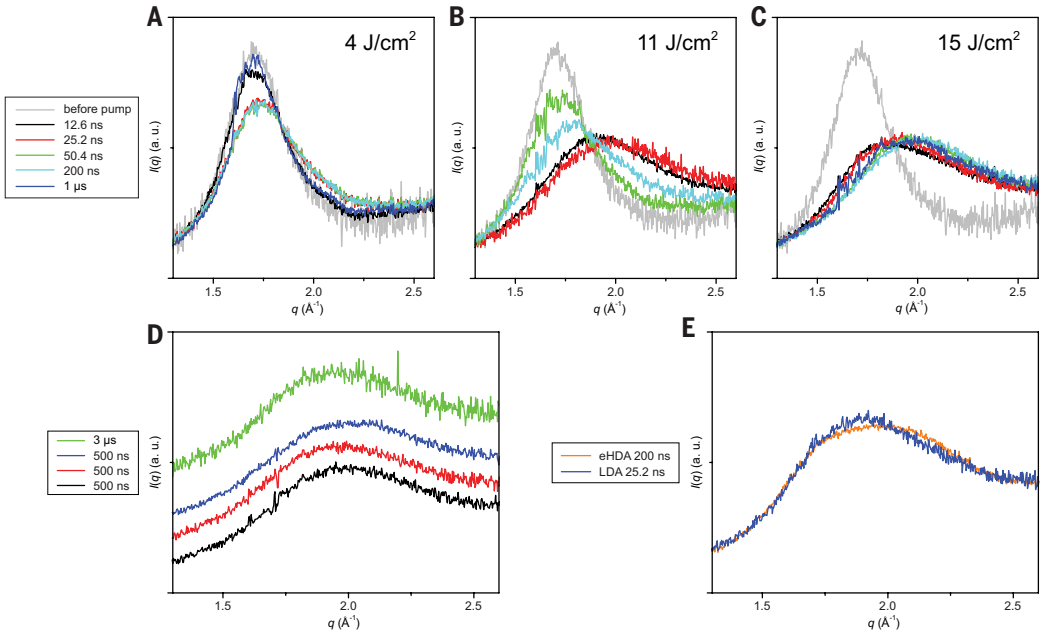

Fig. 4. X-ray scattering during the densification and decompression processes of LDA at different laser fluences. (**A** to **C**) WAXS intensity curves around the first peak in the structure factor at different delays after laser pumping of LDA at laser fluences of 4, 11, and 15 J/cm^2. Small contributions due to Bragg peaks from ice contamination have been removed (fig. S13) (*32*). (**D**) Selected scattering shots at a laser heating fluence of 15 J/cm^2 and a delay of 500 ns plus a single shot at 3 µs. (**E**) Comparison of WAXS intensity curves measured for LDA at a delay of 25 ns and HDA at 200 ns, both at 15 J/cm^2 laser fluence.

indicating coexistence of LDL and HDL (*15*). At 1 µs, the sample decompressed back to LDL, and the estimated temperature based on the data in Fig. 4A was 197 K.

Figure 4B shows the WAXS signal when the fluence is substantially increased to 11 J/cm^2. The time evolution of the WAXS signal was very different from 4 J/cm^2, consistent with the sample entering the high heat capacity regime (Fig. 3B). A complete transformation already occurred by 12 ns, with no trace left of the LDA peak. We observed a broad peak centered at 1.95 to 1.98 Å^{-1}, with a width encompassing both the LDA and HDA positions. The WAXS feature shifted back toward the LDL position through decompression at delays of 50 and 200 ns. The corresponding temperature was ~208 K.

As the fluence increased to 15 J/cm^2, the WAXS signal resembled that at 11 J/cm^2 at earlier times. Using the known relationship between the first peak of the structure factor and density (*37*), we observed that, at both 11 and 15 J/cm^2, there was a rapid increase in density from the initial LDA value, consistent with the wide range of densities, spanning the densities of LDL and HDL, accessible to the sample near the LLCP. Decompression then occurred at later times. The difference between these two higher fluences was that, at 15 J/cm^2, the transition to a lower density by decompression was slower by more than a factor of 10, indicating slower dynamics, even though the temperature was higher. Figure 4D shows selected individual WAXS shots at 0.5 µs as well as a shot at 3 µs, where the system was still in a higher density state, with a broad range of density fluctuations. The WAXS signals for each shot differ to some extent, indicating that the density fluctuations vary at the time of probing. There are a few shots at 30 µs where the higher-density state is maintained alongside 10 to 20% crystallization into hexagonal ice (fig. S25) (*32*). Figure 4E compares the WAXS curves at 15 J/cm^2 obtained from LDA at an early delay time (25.2 ns) and from HDA at the middle of decompression (200 ns). Both show a similar broad WAXS signal, suggesting that both samples pass through a similar regime of critical-like density fluctuations along their respective decompression paths. At this fluence, the temperature was ~210 ± 8 K.

Discussion

When approaching the LLCP, the correlation length should diverge. As described in fig. S10 (*32*), we sought to measure the correlation length using our SAXS data by fitting a Lorentzian function as predicted by Ornstein-Zernike theory (*41*). However, approaching the LLCP from low temperatures triggers domain formation, owing to nucleation or spinodal decomposition, which introduces a strong $1/q^4$ contribution dominating the SAXS signal at low q. This contribution remained strong even at the highest fluences, perhaps due to the temperature gradients in the sample (fig. S11) (*32*). As a result, reliable estimates of the correlation length were not obtained.

When heating HDA, the scattering data in Fig. 2 reveal the progression of thermodynamic behavior depicted in Fig. 1, A and B. At the lowest fluence (3 J/cm^2), a small amount of LDL nucleated from HDL (path T_1 in Fig. 1, A and B), with complete conversion interrupted by crystallization, in agreement with previous HDA pump-probe experiments (*8*). At the next higher fluence (11 J/cm^2), the HDL-to-LDL transition occurred more rapidly and progressed to completion. The SAXS signal was also stronger, indicating the rapid formation of small LDL domains, which then coalesced, consistent with a crossover from nucleation to spinodal decomposition (*42*, *43*). The occurrence of such a crossover means that the sample crossed the HDL spinodal during decompression (path T_2 in Fig. 1, A and B), evidence that the HDL spinodal crosses ambient pressure. The HDL spinodal can only exist at ambient pressure if a LLCP (from which the spinodal emanates) occurs at positive pressure, highlighting how the LLCP determines liquid behavior over a large P-T region. At a fluence of 15 J/cm^2, the scattering signal suggested that the temperature was close to T_c (path T_3 in Fig. 1, A and B). During decompression at T_c, critical fluctuations should occur, although they may be limited in size by the rate at which the system passes through the critical point. The WAXS signal at T_c consists of a single broad peak, consistent with the wide range of densities that are accessible when the HDL and LDL phase basins merge and with interference effects due to cross-correlations between small domains of each phase (fig. S15) (*32*). This broad WAXS peak evolves more slowly than at lower or higher fluence, consistent with the diverging dynamics caused by critical slowing down. The SAXS signal is also at its strongest, indicating a maximum in the density variations monitored in our q window. However, as noted above and in (*32*), a dominant $1/q^4$ scattering contribution in the SAXS made estimation of a correlation length impossible. The scattering signal at a fluence of 20 J/cm^2 indicates heating to a temperature greater than T_c (path T_4 in Fig. 1, A and B). In the supercritical region, only a single phase exists with local fluctuations. The evolution of the scattering peak during decompression resembles that of liquid water under cooling at ambient pressure as well as pressurizing water at ambient temperature (*8*, *40*, *44*). The SAXS signal remains strong, although less so compared with 15 J/cm^2. In summary, the HDA data are consistent with a first-order LLT at low fluence, which becomes continuous at high fluence and hence must pass through the conditions of a LLCP.

When heating LDA, the heat capacity divergence (Fig. 3) indicated that the LLCP occurs at ~210 K, whereas the WAXS data (Fig. 4) at the higher fluences indicated a wide distribution of densities, and an increase in the average density, within a few tens of nanoseconds after heating. These observations are consistent with paths T_2 and T_3 in Fig. 1, D and E, where isochoric heating brings the LDA sample close to the critical conditions, where the density range accessible to the sample spans an average value that is higher than the initial LDA density, and so the density spontaneously increased without the application of additional pressure. On the basis of MD simulations, such a scenario of rapidly accessing the density fluctuations of the LLCP is plausible, with a T_c in the range of 210 K showing density fluctuations on timescales of tens to hundreds of nanoseconds (*25*, *28*, *45*). Furthermore, a recent MD study examined the density variations during rapid isobaric quenching (10 K/ns) of liquid water at 300 K into the glassy state at various pressures and found that there were large density variations of the glass at the critical pressure of the model (*46*). It is also possible that the LDA isochore reached the LDL spinodal, which would trigger HDL formation through spinodal decomposition, again raising the average density without additional pressure. The significant (10-fold) increase in the timescale for relaxation back to the LDL density through decompression when the fluence increased from 11 J/cm^2 to 15 J/cm^2 is consistent with critical slowing down caused by a LLCP, especially given the small difference in temperature (a few kelvin) between these two fluences.

Our observations provide evidence for the existence of a LLCP, the vicinity of which has been directly probed in our experiments. A key remaining question: What is the location of the LLCP in the water phase diagram? The answer has implications for both fundamental and practical applications of the physical properties of water, particularly the formulation of accurate equations of state. Upon heating LDA, we observed a diverging heat capacity with $T_c = 210 \pm 8$ K. We note that the q position for the first peak in the WAXS signal for LDA at 15 J/cm^2 is located at $q = 1.95$ to 1.98 Å^{-1}, depending on the delay; and using the known correlation between the q value of the first peak and the density (*37*), this value would correspond to $\rho_c = 1.023 \pm 0.007$ g/cm^3 (*32*). We estimated the critical pressure using an extrapolated equation of state, and with $T_c = 210 \pm 8$ K and $\rho_c = 1.023 \pm 0.007$ g/cm^3, we find $P_c = 1002 \pm 151$ bar (*31*, *32*). A recent simulation study, using a highly realistic water model based on ab initio quantum calculations, estimated that $T_c = 198$ K and $P_c = 1250$ bar (*27*).

These values are close to recent estimates for the LLCP based on extrapolated thermodynamic data (*31*) giving $T_c = 207$ K, $\rho_c = 1.007$ g/cm^3, and $P_c = 1050$ bar as well as two-state modeling giving $T_c = 218$ to 219 K and $P_c = 580$ to 720 bar (*30*). MD simulations using the TIP4P/2005 model have shown a diverging power law dependence in the isothermal compressibility and correlation length upon cooling toward the critical point at $P_c \approx 1800$ bar and $T_c \approx 170$ K (*9*). However, fitting a power law to the increase of the experimental isothermal compressibility approaching the Widom line, and comparing this to MD simulation results for the TIP4P/2005 model, suggests a downward shift of the LLCP in that model of 700 bar, locating the critical point of real water at approximately 1000 bar and 210 K (*47*). Thus, there is an emerging consensus that the LLCP of supercooled water lies in the vicinity of $T_c = 205$ to 215 K and $P_c = 1000$ bar.

REFERENCES AND NOTES

1. P. G. Debenedetti, *J. Phys. Condens. Matter* **15**, R1669–R1726 (2003).
2. R. J. Speedy, C. A. Angell, *J. Chem. Phys.* **65**, 851–858 (1976).
3. C. A. Angell, W. J. Sichina, M. Oguni, *J. Phys. Chem.* **86**, 998–1002 (1982).
4. C. Huang *et al.*, *J. Chem. Phys.* **133**, 134504 (2010).
5. P. H. Poole, F. Sciortino, U. Essmann, H. E. Stanley, *Nature* **360**, 324–328 (1992).
6. J. C. Palmer *et al.*, *Nature* **510**, 385–388 (2014).
7. P. Gallo *et al.*, *Chem. Rev.* **116**, 7463–7500 (2016).
8. K. H. Kim *et al.*, *Science* **370**, 978–982 (2020).
9. P. G. Debenedetti, F. Sciortino, G. H. Zerze, *Science* **369**, 289–292 (2020).
10. C. A. Angell, *Science* **319**, 582–587 (2008).
11. D. T. Limmer, D. Chandler, *J. Chem. Phys.* **135**, 134503 (2011).
12. O. Mishima, H. E. Stanley, *Nature* **396**, 329–335 (1998).
13. S. Sastry, P. G. Debenedetti, F. Sciortino, H. E. Stanley, *Phys. Rev. E* **53**, 6144–6154 (1996).
14. A. Nilsson, *J. Non-Cryst. Solids X* **14**, 100095 (2022).
15. K. Amann-Winkel *et al.*, *Nat. Commun.* **14**, 442 (2023).
16. K. H. Kim *et al.*, *Science* **358**, 1589–1593 (2017).
17. H. Pathak *et al.*, *Proc. Natl. Acad. Sci. U.S.A.* **118**, e2018379118 (2021).
18. J. A. Sellberg *et al.*, *Nature* **510**, 381–384 (2014).
19. L. Kringle, B. D. Kay, G. A. Kimmel, *J. Chem. Phys.* **159**, 064509 (2023).
20. Y. Xu, H. G. Petrik, R. C. Smith, B. D. Kay, G. A. Kimmel, *Proc. Natl. Acad. Sci. U.S.A.* **113**, 14921–14925 (2016).
21. L. Kringle, W. A. Thornley, B. D. Kay, G. A. Kimmel, *Science* **369**, 1490–1492 (2020).
22. J. Bachler, J. Giebelmann, T. Loerting, *Proc. Natl. Acad. Sci. U.S.A.* **118**, e2108194118 (2021).
23. V. Holten *et al.*, *J. Phys. Chem. Lett.* **8**, 5519–5522 (2017).
24. C. R. Krüger, N. J. Mowry, G. Bongiovanni, M. Drabbels, U. J. Lorenz, *Nat. Commun.* **14**, 2812 (2023).
25. J. Weis, F. Sciortino, A. Z. Panagiotopoulos, P. G. Debenedetti, *J. Chem. Phys.* **157**, 024502 (2022).
26. D. Dhabal, R. Kumar, V. Molinero, *Proc. Natl. Acad. Sci. U.S.A.* **121**, e2322853121 (2024).
27. F. Sciortino, Y. Zhai, S. L. Bore, F. Paesani, *Nat. Phys.* **21**, 480–485 (2025).
28. T. E. Gartner III, P. M. Piaggi, R. Car, A. Z. Panagiotopoulos, P. G. Debenedetti, *Phys. Rev. Lett.* **129**, 255702 (2022).
29. V. Holten, M. A. Anisimov, *Sci. Rep.* **2**, 713 (2012).
30. F. Caupin, M. A. Anisimov, *J. Chem. Phys.* **151**, 034503 (2019).
31. O. Mishima, T. Sumita, *J. Phys. Chem. B* **127**, 1414–1421 (2023).
32. Details of the materials and methods, as well as supporting analysis of the experimental and theoretical data, are available in the supplementary materials.
33. F. Sciortino, T. E. Gartner 3rd, P. G. Debenedetti, *J. Chem. Phys.* **160**, 104501 (2024).
34. E. M. Mollica, J. Russo, H. E. Stanley, F. Sciortino, *J. Non-Cryst. Solids X* **13**, 100081 (2022).
35. D. Mariedahl *et al.*, *J. Phys. Chem. B* **122**, 7616–7624 (2018).
36. F. Perakis *et al.*, *Proc. Natl. Acad. Sci. U.S.A.* **114**, 8193–8198 (2017).
37. T. Loerting *et al.*, *J. Phys. Chem. B* **115**, 14167–14175 (2011).
38. M. Ladd-Parada *et al.*, *J. Phys. Chem. B* **126**, 2299–2307 (2022).
39. L. B. Skinner, C. J. Benmore, J. C. Neuefeind, J. B. Parise, *J. Chem. Phys.* **141**, 214507 (2014).
40. N. Esmaeildoost *et al.*, *J. Chem. Phys.* **155**, 214501 (2021).
41. H. E. Stanley, *Introduction to Phase Transitions and Critical Phenomena* (Oxford Univ. Press, 1971).
42. J. W. Cahn, *J. Chem. Phys.* **42**, 93–99 (1965).
43. F. Sciortino, R. Bansil, H. E. Stanley, P. Alström, *Phys. Rev. E* **47**, 4615–4618 (1993).
44. L. B. Skinner *et al.*, *J. Chem. Phys.* **144**, 134504 (2016).
45. T. A. Kesselring, G. Franzese, S. V. Buldyrev, H. J. Herrmann, H. E. Stanley, *Sci. Rep.* **2**, 474 (2012).
46. R. J. Szukalo, N. Giovambattista, P. G. Debenedetti, *Proc. Natl. Acad. Sci. U.S.A.* **122**, e2509609122 (2025).
47. A. Späh *et al.*, *Phys. Chem. Chem. Phys.* **21**, 26–31 (2018).
48. S. You *et al.*, Experimental evidence of a liquid-liquid critical point in supercooled water [Dataset], Dryad (2025); https://doi.org/10.5061/dryad.pc866t23j.

ACKNOWLEDGMENTS

Funding: This work was supported by National Research Foundation of Korea (NRF) grants funded by the Korean government (MSIT) (nos. RS-2020-NR049542 and RS-2024-00348773), the Samsung Science and Technology Foundation (SSTF-BA2002-07), the Swedish National Research Council (2013-8823 and 2023-5080), the Ragnar Söderbergs Stiftelse, and the Natural Sciences and Engineering Research Council of Canada (NSERC, RGPIN-2024-04477). The experiments were performed using the XSS-FXL beamline at PAL-XFEL (proposal nos. 2021-2nd-XSS-015, 2022-1st-XSS-017, and 2022-2nd-XSS-015) funded by the Ministry of Science and ICT of Korea. **Author contributions:** A.N. and K.H.K. designed and supervised the study. K.A.-W. designed sample preparation. M.L.-P., A.K., R.T., S.L., and K.N. prepared amorphous ice samples. K.H.K., A.N., K.A.-W., and F.P. designed the experimental setup, chamber, and laser geometry. K.H.K., A.N., S.Y., M.L.-P., K.N., A.K., M.S., C.Y., Y.H., S.J., S.L., K.P., K.K., M.Ki, R.T., J.H.L., I.E., M.Kim, R.M., and D.J. performed the x-ray experiments. P.H.P., K.R., S.Y., I.A., and F.P. performed the computer simulations. S.Y., K.H.K., A.N., and P.H.P. analyzed the data. A.N., K.H.K., S.Y., P.H.P., M.L.-P., K.A.-W., and F.P. wrote the manuscript, with input from all coauthors. **Competing interests:** The authors declare that they have no competing interests. **Data, code, and materials availability:** All data necessary for evaluating the conclusions of the study are available at Dryad (*48*).

SUPPLEMENTARY MATERIALS

science.org/doi/10.1126/science.aec0018
Materials and Methods; Supplementary Text; Figs. S1 to S25; References (*49*–*59*)

Submitted 3 September 2025; accepted 8 January 2026

10.1126/science.aec0018

Experimental evidence of a liquid-liquid critical point in supercooled water

Seonju You, Marjorie Ladd-Parada, Kyeongmin Nam, Aigerim Karina, Seoyoung Lee, Myeongsik Shin, Cheolhee Yang, Yeseul Han, Sangmin Jeong, Kichan Park, Kyeongwon Kim, Minjeong Ki, Robin Tyburski, Iason Andronis, Keely Ralf, Jae Hyuk Lee, Intae Eom, Minseok Kim, Rory Ma, Dogeun Jang, Fivos Perakis, Peter H. Poole, Katrin Amann-Winkel, Kyung Hwan Kim, and Anders Nilsson

Science **391** (6792), . DOI: 10.1126/science.aec0018

Editor's summary

Polyamorphism and the resulting liquid-liquid critical point (LLCP) in supercooled water are intriguing phenomena in condensed-matter science. Rapid spontaneous ice formation that the water can undergo when probed makes finding the LLCP extremely challenging experimentally. Previously, evidence for polyamorphism relied on indirect signs such as extrapolating unusual physical properties, the presence of two amorphous ice forms, and liquid-liquid transitions in simulations. Experiments presented by You *et al*. with isochoric heating of high- and low-density amorphous ices using infrared ultrafast laser pulses followed by x-ray scattering at time scales before ice formation have directly and convincingly demonstrated two liquid states near a critical point in supercooled water (see the Perspective by Paesani). —Yury Suleymanov

Science (ISSN 1095-9203) is published by the American Association for the Advancement of Science. 1200 New York Avenue NW, Washington, DC 20005. The title *Science* is a registered trademark of AAAS.